NASA/TM–1998–208738

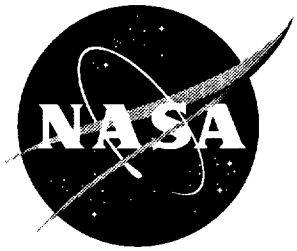

Comments on the Diffusive Behavior of Two Upwind Schemes

William A. Wood and William L. Kleb
Langley Research Center, Hampton, Virginia

National Aeronautics and
Space Administration

Langley Research Center
Hampton, Virginia 23681–2199

October 1998

Available from:

NASA Center for AeroSpace Information (CASI)
7121 Standard Drive
Hanover, MD 21076–1320
(301) 621–0390

National Technical Information Service (NTIS)
5285 Port Royal Road
Springfield, VA 22161–2171
(703) 605–6000

Abstract

The diffusive characteristics of two upwind schemes, multi-dimensional fluctuation splitting and locally one-dimensional finite volume, are compared for scalar advection-diffusion problems. Algorithms for the two schemes are developed for node-based data representation on median-dual meshes associated with unstructured triangulations in two spatial dimensions. Four model equations are considered: linear advection, non-linear advection, diffusion, and advection-diffusion. Modular coding is employed to isolate the effects of the two approaches for upwind flux evaluation, allowing for head-to-head accuracy and efficiency comparisons. Both the stability of compressive limiters and the amount of artificial diffusion generated by the schemes is found to be grid-orientation dependent, with the fluctuation splitting scheme producing less artificial diffusion than the finite volume scheme. Convergence rates are compared for the combined advection-diffusion problem, with a speedup of 2.5 seen for fluctuation splitting versus finite volume when solved on the same mesh. However, accurate solutions to problems with small diffusion coefficients can be achieved on coarser meshes using fluctuation splitting rather than finite volume, so that when comparing convergence rates to reach a given accuracy, fluctuation splitting shows a speedup of 29 over finite volume.

Nomenclature

A, B	Flux Jacobians
c	Nodal update coefficients
$\vec{F}$	Convective flux vector, $\vec{F} = \vec{F}(x, y, u)$
h	Mesh spacing
$\hat{\imath}, \hat{\jmath}$	Cartesian unit vectors
J^{-1}	Inverse Jacobian of the coordinate transformation
ℓ	Edge length
M	Averaging function for limiters
$\hat{n}$	Outward unit normal to control cell
$\mathbf{n}$	Length-scaled inward normal
Q	Fluctuation ratio
$\vec{r}$	Distance vector from node to face
S_i	Median-dual area about node i
t	Time
u	Dependent variable
x, y	Cartesian coordinates
α, β	Curvilinear advection speeds
Γ	Boundary of control cell
γ	Limiter bound
ε	Small parameter for van Albada limiter
ϑ	Finite element linear shape function
$\vec{\lambda}$	Advection velocity vector

ν	Diffusion coefficient
ξ, η	Curvilinear coordinates
τ	Timestep
$\bar{\phi}^{\xi}, \bar{\phi}^{\eta}$	Artificial dissipation—fluctuation splitting
Φ	Artificial dissipation—finite volume
ϕ	Element advective fluctuation
ϕ^{ξ}, ϕ^{η}	Fluctuation components
$\phi^{\xi^*}, \phi^{\eta^*}$	Limited fluctuations
ϕ_v	Viscous fluctuation
ψ	Limiter function
Ω	Area of control cell
∇	Gradient operator

Introduction

Upwind discretizations for advection equations typically introduce artificial numerical dissipation into the solution. When combined advection-diffusion problems are considered, this dissipation introduced in the discretization of the advection terms should be less than the true physical diffusion. To this end the diffusive characteristics of upwind schemes are investigated and their performance in resolving solutions to advection-diffusion problems with small diffusion coefficients is analyzed.

Two node-based, median-dual methods for modeling convective fluxes are considered. The first is a traditional locally one-dimensional approximate Riemann solver finite volume (FV) scheme.[1] Locally one-dimensional schemes applied on multidimensional domains are known to introduce excess dissipation when discontinuities are not aligned with the mesh.[2]

The second method is the NNL[3] fluctuation splitting (FS) scheme, also referred to in the literature as a residual distribution scheme. FS has a more-compact stencil than FV for second-order formulations and exhibits "zero cross-diffusion"† in a grid-aligned condition. Both of these attributes should lead to less introduced dissipation as compared with FV.

The sensitivity of FS to grid orientation and resulting production of cross-diffusion is investigated in the present report. The use of compressive limiter functions is also tested with both algorithms. Local timesteps based on positivity arguments are implemented for both first- and second-order discretizations of the implicit matrix.

Formulation of FS schemes for diffusion problems is a recent research area.[4,5] The present study seeks to quantify the relative merits of using a low-diffusion advection operator to resolve advection-diffusion problems with small diffusion coefficients. Lessons learned on these problems will guide the development of computer codes for solving compressible viscous fluid dynamic problems. A similar approach for central difference schemes with explicit numerical dissipation has recently been taken by Efraimsson.[6]

† "Zero cross diffusion" refers to the practice of adding artificial diffusion terms in the streamwise direction only, as opposed to adding artificial dissipation in both the streamwise and cross-stream directions.

Governing Equations

The non-linear advection-diffusion equation,

$$u_t + \nabla \cdot \vec{F} = \nabla \cdot (\nu \nabla u) \tag{1}$$

is cast as a hyperbolic conservation law, to which steady-state solutions are sought.

Finite Volume

In FV form, using the divergence theorem Eqn. 1 becomes,

$$\int_\Omega u_t \, d\Omega = - \oint_\Gamma (\vec{F} - \nu \nabla u) \cdot \hat{n} \, d\Gamma \tag{2}$$

where Ω is the median dual about node i and Γ is the boundary of Ω. Using mass lumping to the nodes, similar to an explicit finite element treatment,[8] the temporal evolution is evaluated on a time-invariant mesh as,

$$\int_\Omega u_t \, d\Omega = S_i \frac{\partial u_i}{\partial t} \rightarrow \frac{S_i}{\tau} \left(u_i^{t+\tau} - u_i^t \right) \tag{3}$$

The discretization of the convective flux, $\vec{F}$, is performed using Barth's implementation[1] of the upwind, locally one-dimensional, approximate Riemann solver of Roe.[9]

$$\oint_\Gamma \vec{F} \cdot \hat{n} \, d\Gamma \rightarrow \sum_{faces} \left[\frac{1}{2} \left(\vec{F}_{in} + \vec{F}_{out} \right) \cdot \hat{n} - \Phi \right] \Delta\Gamma \tag{4}$$

where the artificial dissipation provides the upwinding,

$$\Phi = \frac{1}{2} |\tilde{A} \hat{n}_x + \tilde{B} \hat{n}_y| (u_{out} - u_{in}) \tag{5}$$

with $\hat{n} = \hat{n}_x \hat{\imath} + \hat{n}_y \hat{\jmath}$. *Out* and *in* refer to states on the outside and inside of Ω at the face. A and B are the flux Jacobians,

$$A = \frac{\partial F^{(1)}}{\partial u}, \qquad B = \frac{\partial F^{(2)}}{\partial u} \tag{6}$$

and $(\tilde{A}, \tilde{B})$ represent their conservative linearizations at the cell face.[9]

Piecewise linear reconstruction from the nodal unknowns to the cell faces as,

$$u_{face} = u_i + \psi \nabla u \cdot \vec{r} \tag{7}$$

provides second-order spatial accuracy in smoothly-varying regions of the solution. Median-dual gradients of the dependent variable, ∇u, are obtained from the unweighted least squares procedure outlined by Barth. Following Bruner and Walters,[14] the limiter is supplied an argument equal to half the argument Barth uses, namely,

$$\psi = \psi \left(\frac{u^{min/max} - u_i}{2(\nabla u \cdot \vec{r})^{min/max}} \right) \tag{8}$$

where $u^{min/max}$ is the minimum (resp. maximum) of u_i and all distance-one neighbors. The most restrictive limiting from choosing the minimum or maximum is used.

In casting the limiter argument in this form, Bruner equates the Barth limiter with Superbee, for a limiter argument less than or equal to one. The present authors incorrectly identified the Barth limiting with the non-symmetric Chakravarthy and Osher[13] limiter in Ref. 7. The Barth limiting is non-symmetric, but takes the form,

$$\psi\left(\frac{p}{q}\right) = \begin{cases} 0 & \frac{p}{q} \leq 0 \\ 2\frac{p}{q} & \text{if} \quad 0 < \frac{p}{q} < \frac{1}{2} \\ 1 & \frac{p}{q} \geq \frac{1}{2} \end{cases} \tag{9}$$

for the limiter cast as Eqn. 8.

Two methods for evaluating the diffusion term are incorporated into FV. The more compact of the two, the finite element discretization, is discussed in the following section. The less-compact diffusion formula is obtained by discretizing the last term of Eqn. 2, in a manner similar to Eqn. 4,

$$\oint_\Gamma \nu \nabla u \cdot \hat{n}\, d\Gamma \rightarrow \sum_{faces} \frac{\bar{\nu}}{2} \left(\nabla u_{in} + \nabla u_{out}\right) \cdot \hat{n}\, \Delta\Gamma \tag{10}$$

The diffusion coefficient is averaged over the length of the face. The gradients from Eqn. 7 are not limited before averaging at the control-volume faces in Eqn. 10, as suggested by Anderson and Bonhaus.[10]

Fluctuation Splitting

The NNL FS scheme is presented as a slight re-interpretation of the work of Sidilkover and Roe.[3] The current interpretation is as a volume integral over triangular elements, without recourse to the divergence theorem. The discretized equations, however, are identical.

Integrating Eqn. 1 over an element, where Ω is now the area of the triangular element,

$$\int_\Omega u_t\, d\Omega = -\int_\Omega \nabla \cdot \vec{F}\, d\Omega + \int_\Omega \nabla \cdot (\nu \nabla u)\, d\Omega \tag{11}$$

For linear variation of the dependent variable over the element, the temporal evolution is,

$$\int_\Omega u_t\, d\Omega = \Omega \bar{u}_t = \frac{\Omega}{3}(u_{1_t} + u_{2_t} + u_{3_t}) \tag{12}$$

where u_1, u_2, and u_3 correspond to the three nodes defining element Ω.

Defining local curvilinear coordinates, ξ and η, parallel to sides $\overline{12}$ and $\overline{23}$, respectively (Fig. 1), the divergence of the convective flux can be written,

$$\nabla \cdot \vec{F} = F_x^{(1)} + F_y^{(2)} = \frac{1}{J^{-1}} \left(\hat{n}_2 \cdot \vec{F}_\xi - \hat{n}_1 \cdot \vec{F}_\eta\right) \tag{13}$$

Defining the scaled inward normal, $\mathbf{n} = -h\hat{n}$, where h is a mesh edge length, the divergence (Eqn. 13) becomes,

$$\nabla \cdot \vec{F} = \frac{1}{2\Omega} \left(-h_{12}\mathbf{n}_2 \cdot \vec{F}_\xi + h_{23}\mathbf{n}_1 \cdot \vec{F}_\eta\right) \tag{14}$$

If $\vec{F}$ is linear or quadratic in u, then for a linear variation of u over the element,

$$\int_\Omega \nabla \cdot \vec{F}\, d\Omega = \alpha \Delta_{21} u + \beta \Delta_{32} u \tag{15}$$

where the difference operator is defined $\Delta_{21} u = u_2 - u_1$ and the advection speeds are,

$$\alpha = -\frac{1}{2}(\mathbf{n}_{2_x}\tilde{A} + \mathbf{n}_{2_y}\tilde{B}), \quad \beta = \frac{1}{2}(\mathbf{n}_{1_x}\tilde{A} + \mathbf{n}_{1_y}\tilde{B}) \tag{16}$$

$\tilde{A}$ and $\tilde{B}$ are now the conservative linearizations over the triangular element.[11]

The advective fluctuation can be defined,

$$\phi = -\int_\Omega \nabla \cdot \vec{F}\, d\Omega \tag{17}$$

The fluctuation can be split,

$$\phi = \phi^\xi + \phi^\eta \tag{18}$$

where,

$$\phi^\xi = -\alpha \Delta_{21} u, \quad \phi^\eta = -\beta \Delta_{32} u \tag{19}$$

Following Sidilkover[12] the fluctuation is limited to achieve a second-order scheme,

$$\phi^{\xi^*} = \phi^\xi + \phi^\eta \psi(Q) = \phi^\xi \left(1 - \frac{\psi(Q)}{Q}\right) \tag{20}$$

$$\phi^{\eta^*} = \phi^\eta - \phi^\eta \psi(Q) = \phi^\eta \left(1 - \psi(Q)\right) \tag{21}$$

with,

$$Q = -\frac{\phi^\xi}{\phi^\eta} \tag{22}$$

Upwinding is achieved through the introduction of the artificial dissipation terms,

$$\bar{\phi}^\xi = \text{sign}(\alpha)\phi^{\xi^*}, \quad \bar{\phi}^\eta = \text{sign}(\beta)\phi^{\eta^*} \tag{23}$$

Combining Eqn. 12 with a distribution scheme for Eqn. 17 and summing over all elements, the contributions to nodal time derivatives can be written in the form,

$$\begin{aligned}
S_1 u_{1_t} &\leftarrow \frac{1}{2}(\phi^{\xi^*} - \bar{\phi}^\xi) + COE \\
S_2 u_{2_t} &\leftarrow \frac{1}{2}(\phi^{\xi^*} + \bar{\phi}^\xi) + \frac{1}{2}(\phi^{\eta^*} - \bar{\phi}^\eta) + COE \\
S_3 u_{3_t} &\leftarrow \frac{1}{2}(\phi^{\eta^*} + \bar{\phi}^\eta) + COE
\end{aligned} \tag{24}$$

or in a more compact form,

$$S_i u_{i_t} \leftarrow \frac{1}{4}\left[i(3-i)(\phi^{\xi^*} + (-1)^i \bar{\phi}^{\xi}) + (-4+5i-i^2)(\phi^{\eta^*} - (-1)^i \bar{\phi}^{\eta})\right] + COE \tag{25}$$

where COE stands for contributions from other elements containing these nodes.

A finite element treatment, similar to Tomaich,[4] is employed to obtain the diffusive fluctuation,

$$\phi_v = \int_\Omega \nabla \cdot (\nu \nabla u)\, d\Omega \tag{26}$$

Assuming piecewise-linear data and an element-averaged diffusion coefficient leads to a diffusive fluctuation of zero for the triangular element. Introducing the linear nodal shape functions ϑ_i, such that $\sum_{i=1}^{3} \vartheta_i = 1$, the elemental diffusive fluctuation can be expressed $\phi_v = \sum_{i=1}^{3} \phi_{v_i} = 0$, where

$$\phi_{v_i} = \int_\Omega \vartheta_i \nabla \cdot (\bar{\nu} \nabla u)\, d\Omega \tag{27}$$

Integrating by parts,

$$\phi_{v_i} = \oint_\Gamma \vartheta_i \bar{\nu} \nabla u \cdot \hat{n}\, d\Gamma - \int_\Omega \bar{\nu} \nabla u \cdot \nabla \vartheta_i\, d\Omega \tag{28}$$

The boundary integral in Eqn. 28 will cancel on summing contributions for interior nodes. The remaining volume integral can be evaluated analytically,

$$\phi_{v_i} = -\frac{\bar{\nu}}{2} \nabla u \cdot \mathbf{n}_{i+1} = -\frac{\bar{\nu}}{4\Omega} \sum_{j=1}^{3} u_j \mathbf{n}_{j+1} \cdot \mathbf{n}_{i+1} \tag{29}$$

Distributing this diffusive fluctuation to the nodes and keeping only the larger of the physical or artificial dissipation leads to the update formula,

$$\begin{aligned}
S_1 u_{1_t} &\leftarrow \frac{\phi^{\xi^*}}{2} + \max\left(-\frac{\bar{\phi}^{\xi}}{2}, \phi_{v_1}\right) + COE \\
S_2 u_{2_t} &\leftarrow \frac{\phi^{\xi^*} + \phi^{\eta^*}}{2} + \max\left(\frac{(\bar{\phi}^{\xi} - \bar{\phi}^{\eta})}{2}, \phi_{v_2}\right) + COE \\
S_3 u_{3_t} &\leftarrow \frac{\phi^{\eta^*}}{2} + \max\left(\frac{\bar{\phi}^{\eta}}{2}, \phi_{v_3}\right) + COE
\end{aligned} \tag{30}$$

Boundary Conditions

Explicit Dirichlet inflow boundary conditions are employed. Advective outflow boundaries are treated for free convection through the boundary nodes, allowing boundary nodes to be handled in the same manner as interior nodes. For the diffusion terms a Neumann outflow boundary is applied with zero gradient, achieved by setting the boundary integral in Eqn. 28 to zero.

Limiter functions

Minmod, van Albada,[15] Superbee, and γ[16] symmetric limiters are utilized for FV (Eqn. 7) and FS (Eqns. 20 and 21) in the form of symmetric averaging functions related to the limiter as,

$$q\,\psi\left(\frac{p}{q}\right) = M(p,q) = M(q,p) = p\,\psi\left(\frac{q}{p}\right)$$

The van Albada averaging function is,

$$M = \frac{(pq+\varepsilon^2)(p+q)}{p^2+q^2+2\varepsilon^2}$$

where the small parameter ε varies like $\varepsilon^2 \sim \Delta x^3$, and serves to reduce the limiting in smooth regions.

The averaging function for the γ limiter, of which the Minmod ($\gamma = 1$) and Superbee ($\gamma = 2$) are special cases, is,

$$M(p,q) = \begin{cases} 0 & pq \le 0 \\ \gamma p & \gamma|p| \le |q| \\ q & \text{if } |p| \le |q| \le \gamma|p| \\ p & |q| \le |p| \le \gamma|q| \\ \gamma q & \gamma|q| \le |p| \end{cases} \tag{31}$$

Timestep

Both schemes are formulated either as Gauss-Seidel time-relaxation or forward Euler time-evolution algorithms.

The nodal updates for the discrete system can be formed as a sum of contributions from all nodes.

$$u_i^{t+\tau} = \sum_j c_j u_j = c_i u_i + \sum_{j\neq i} c_j u_j \tag{32}$$

For positivity[17] each of the coefficients in Eqn. 32 must be non-negative.

Advective Timestep restriction

In the FV context the nodal update (Eqn. 32) can be rearranged into the form of Eqn. 3,

$$\frac{S_i}{\tau}(u_i^{t+\tau} - u_i^t) = \frac{S_i}{\tau}(c_i - 1)u_i + \frac{S_i}{\tau}\sum_{j\neq i} c_j u_j \tag{33}$$

For the upwind, edge-based algorithm considered here, each $\frac{S_i}{\tau}c_j$ will be related to a positive-definite coefficient equal to zero for outflowing faces and related to the wavespeed for inflowing faces, yielding the restriction $\tau \ge 0$ on the timestep. The remaining term can be

expressed,

$$\frac{S_i}{\tau}(c_i - 1) = -\sum_{k \text{ about } i} c_k \tag{34}$$

where the c_k coefficients are also positive-definite, either zero for inflowing faces or related to the wavespeed for outflowing faces. Rearranging and imposing the positivity constraint, $c_i \geq 0$, yields the timestep restriction,

$$1 - \frac{\tau}{S_i}\sum_{k \text{ about } i} c_k = c_i \geq 0 \tag{35}$$

$$\tau \leq \frac{S_i}{\sum_{k \text{ about } i} c_k} \tag{36}$$

For FS, the nodal updates are assembled from Eqn. 24 as,

$$\frac{S_i}{\tau}(u_i^{t+\tau} - u_i^t) = \sum_{j \neq i} c_j (u_j - u_i) \tag{37}$$

In this case the c_j coefficients are formed as contributions from the fluctuations in the triangles to both the left and the right of mesh edge $\overline{ij}$. The positivity restriction on τ is found to have a similar form as for finite volume (Eqn. 36),

$$\tau \leq \frac{S_i}{\sum_{j \neq i} c_j} \tag{38}$$

Local time-stepping based on positivity is shown to yield stable, yet non-converging, solutions in some second-order cases (see Results section). Robust convergence is obtained by using the first-order c's in Eqns. 36 and 38, even for second-order-accurate spatial discretizations. This is equivalent to the common practice of using a first-order Jacobian discretization in an time-implicit scheme.

Diffusive Timestep Restriction

Unfortunately, the finite element formulation for the diffusive terms (Eqn. 29) cannot be guaranteed to preserve local positivity on obtuse triangles (see Barth[1]). Considering only the contributions from the current node, the coefficient for the diffusion term can be written,

$$u_i^{t+\tau} = u_i^t \left(1 - \frac{\tau}{S_i}\sum_T \frac{\nu \ell^2}{4\Omega}\right) \tag{39}$$

The appropriate edge length is the side of the element opposite the current node. The resulting timestep restriction is,

$$\tau \leq \frac{S_i}{\sum_T \frac{\nu \ell^2}{4\Omega}} \tag{40}$$

In a similar manner the timestep restriction from Eqn 10 is,

$$\tau \leq \frac{S_i}{\sum_T \frac{3\nu \Delta\Gamma^2}{4\Omega}} \tag{41}$$

Results

Linear Advection

The linear advection equation is obtained from Eqn. 1 by setting $\nu = 0$ and $\vec{F} = \vec{\lambda}u$, yielding,

$$u_t + \nabla \cdot (\vec{\lambda}u) = 0 \tag{42}$$

A divergence-less advection velocity is considered, such that $\nabla \cdot \vec{\lambda} = 0$. Equation 42 can then be written,

$$u_t + \vec{\lambda} \cdot \nabla u = 0 \tag{43}$$

Uniform Advection

Uniform advection of the Heavyside function at -45 degrees, $\vec{\lambda} = (1, -1)$, on a cut-cartesian mesh is shown for first-order FS, second-order FS, and second-order FV in Figs. 2–4, respectively. The mesh is shown as the dashed background, and equally-spaced contours vary on [0,1], the minimum and maximum solution values. The spread of the contour lines with spatial evolution is indicative of the amount of dissipation introduced into the solution by the discretization of the convective terms.

Second-order FS is seen to be greatly superior to first-order, as expected, reproducing the exact solution in this case with no introduced dissipation. Also, FS represents a significant reduction in numerical diffusion versus the corresponding FV scheme, with both results employing the Minmod limiter.

However, the "zero cross-diffusion" results of Fig. 3 with FS are misleading. In Fig. 5 the advection velocity has been rotated counter clockwise by 90 degrees on the same grid. Clearly, the artificial dissipation introduced by the FS scheme has been increased.

The corresponding FV solution is shown in Fig. 6. While the change in contour spreading for the FV scheme between Figs. 4 and 6 is less dramatic than the change in spreading for the FS scheme in Figs. 3 and 5, the FS results still exhibit less diffusion than the FV results, comparing Figs. 5 and 6.

Employing the compressive Superbee limiter with the FS scheme yields the results of Fig. 7. In this case the discontinuity is confined to a 2–3 cell stencil, and does not grow in space. Applying the Superbee limiter to FV cannot eliminate all artificial dissipation for this case, as is possible with FS. The FV results (not shown) corresponding to Fig. 7 spread the discontinuity over four cells by the outflow boundary, with a continually broadening trend.

However, while it is possible to use the Superbee limiter with FS for this case, compressive limiters can be unstable on different grid orientations. For example, no degree of compression is stable for the case of Fig. 3. This potential for instability is related to global positivity, as discussed by Sidilkover and Roe.[3]

The effect of using a general unstructured grid is investigated in Figs. 8 and 9. The unstructured grid in this case was generated using VGRID.[18,19] The FS solution exhibits less dissipation, but is not as smooth as the FV solution. While the FS scheme preserves contact discontinuities over larger spatial ranges than the FV scheme, FS does not appear to degenerate gracefully with regard to extreme coarsening of the unstructured mesh for this test case. This behavior could have negative implications for applications employing multigrid convergence acceleration.

Circular Advection

Circular advection is achieved by setting $\vec{\lambda} = (y, -c)$. A decaying sine-wave input profile is used,

$$u(x,0) = (e^x \sin \pi x)^2$$

Results for the two schemes, using the Minmod limiter, are presented on the worse-case cut-cartesian mesh in Figs. 10 and 11. Again, the FS results are considerably less diffusive than the FV solution.

The circular-advection problem is also applied on an unstructured mesh. The input profile for this case consists of both a top-hat function and a decaying sine wave, allowing comparisons between the schemes for both sharp discontinuities and smooth gradients. The input profile is,

$$u(x,0) = \begin{cases} (e^{2x} \sin(2\pi x))^2 & -0.5 \leq x < 0 \\ 0 & -0.6 \leq x < -0.5 \\ 0.4 & -0.8 \leq x < -0.6 \\ 0 & -1 \leq x < -0.8 \end{cases}$$

Results for this case are displayed in Fig. 12 for FS and Fig. 13 for FV, both using the Minmod limiter. FS performs significantly better at preserving the top-hat distribution. FS also does a better job of maintaining the minimum and maximum values of the sine distribution, though both schemes do well on the smooth gradient portion of the sine wave.

Non-linear Advection

The non-linear advection equation is obtained from Eqn. 1 by setting $\vec{F} = (\frac{u^2}{2}, u)$ with $\nu = 0$. In non-conservative form the equation is written,

$$u_t + uu_x + u_y = 0$$

A coalescing shock problem is considered, with an anti-symmetric input profile,

$$u(-1,y) = u(0,y) = 0$$

$$u(x,0) = -2x - 1 \text{ on } x = (-1,0)$$

The exact solution to this problem contains symmetric expansion fans on the sides and a compression fan at the inflow that coalesces into a vertical shock at $(x,y) = (-\frac{1}{2}, \frac{1}{2})$.

The first mesh is cut-cartesian containing 26×26 nodes. The FS and FV solutions, both using the Minmod limiter, are presented in Figs. 14 and 15. Both algorithms exhibit the same grid dependence on the amount of artificial dissipation as seen before, with the left-half solutions having more diffusion than the right halves, due to the grid orientation. Both methods perform the same in the compression-fan region, coalescing into a shock to within the accuracy of the input-profile discretization.

The shock is more sharply defined by FS than by FV. Figure 14 has the correct shock speed, with nearly the entire gradient captured in one cell thickness. In contrast, Fig. 15

shows a slightly incorrect shock speed when using FV, as the shock progresses to the left beyond the coalescence point, even though the discretization is conservative. The incorrect shock speed results from a non-symmetric distribution of the dependent variable to the left and right of the shock, caused by the excessive artificial diffusion generated on the grid-misaligned (left-hand) side.

Contours of the absolute value of the error are presented in Figs. 16 and 17. Errors from both computed solutions show a lack of symmetry, again reflecting the grid dependence of the artificial diffusion terms. The error levels from FS are less than from FV. The shock curvature in the FV solution at the coalescing point is clearly visible in Fig. 17, resulting in significant downstream errors in the shock location as compared with the FS errors.

This problem is repeated on a 25×25 mesh with symmetric diagonal cuts, favorably aligned with the advection directions. The FS and FV solutions, Figs. 18 and 19, are in good agreement. Plots of the absolute error contours, Figs. 20 and 21, show FS to be a little more accurate than FV for this case.

The final mesh for this case is a truly unstructured triangulation containing 847 nodes and 1617 cells. The nodes are clustered to the outflow boundary, with a bias towards the left-hand side. The FS solution is presented in Fig. 22, showing very accurate and crisp shock resolution and good symmetry in the solution contours despite the mesh-clustering bias. In contrast, the FV solution in Fig. 23 has a more-diffuse shock and again an incorrect shock speed, with the outflow shock offset to the left of $x = -\frac{1}{2}$. The FV solution is also somewhat less symmetric than the FS solution.

Linear Diffusion

Choosing $\vec{F} = 0$, the heat-conduction equation is obtained from Eqn. 1,

$$u_t = \nabla \cdot (\nu \nabla u)$$

The test problem, a steady-state boundary value problem on a unit square, is taken from Tomaich.[4] The Dirichlet boundary values are,

$$u(-1, y) = 0, \qquad u(0, y) = \sin(\pi y)$$

$$u(x, 0) = 0, \qquad u(x, 1) = -\sin(\pi x)$$

The analytical solution on $x = [-1, 0]$, $y = [0, 1]$ is,

$$u(x, y) = \frac{1}{\sinh \pi} \left[\sinh(\pi(x+1)) \sin(\pi y) + \sinh(\pi y) \sin(\pi(x+1))\right]$$

Both diffusion discretizations, Eqns. 10 and 29, are compared on a 438-node unstructured mesh. Figures 24 and 25 plot the absolute value of the error in the converged solutions using Eqns. 10 and 29, respectively. A carpet plot of the solution, using the finite element formulation, is presented in Fig. 26.

The finite element treatment is clearly more accurate, and is used to discretize the diffusion terms for both FV and FS in the following section. The average-gradient results in Fig. 24 appear to exhibit a decoupling mode, similar to odd/even decoupling for structured meshes.

Linear Advection-Diffusion

The final test case is a linear advection-diffusion problem of Smith and Hutton.[20] The flux function is $\vec{F} = \vec{\lambda}u$, with,

$$\vec{\lambda} = \left(2y(1-x^2),\ -2x(1-y^2)\right)$$

The streamlines for this problem, while not truly circular, are similar in orientation to the circular advection problem. The inflow profile is,

$$u(x,0) = 1 + \tanh(20x + 10)$$

The diffusion coefficient is chosen to be a constant, $\nu = 10^{-3}$. The domain is the unit square in the second quadrant. No closed-form solution is known to the authors for this problem.

A sequence of five unstructured meshes is considered. The meshes have no preferred clustering or stretching and have nominal node-spacings of 0.1, 0.05, 0.025, 0.0125, and 0.00625, labeled as Meshes A–E, respectively. The number of nodes for each mesh, along with the solution times for both FS and FV on a 195 MHz SGI R10000 CPU are listed in Table 1.

L_2-norms of the artificial and physical viscosities computed using both FS and FV are presented for each mesh in Table 2. Notice that the norm of the artificial dissipation for both FV and FS drops lower than the norm of the physical dissipation on Meshes D and E. Since the algorithms select only the larger of the physical or artificial dissipation (Eqn. 30), Table 2 suggests both schemes are grid resolved on Mesh D. However, the norm of the physical dissipation is smaller for FV than FS on each mesh A–D. The physical viscosity is driven by the solution curvature, suggesting FS maintains the solution profile sharper than FV on the coarser meshes. A comparison of outflow profiles will soon verify this interpretation.

Further evidence of a grid-resolved FS solution is seen in Figs. 27 and 28. The FS solution on Mesh E at the outflow boundary is presented along with the inflow profile and the corresponding pure-advection ($\nu = 0$) FS solution in Fig. 27. The pure-advection solution is seen to replicate the inflow profile, with a clear separation from the diffused, $\nu = 10^{-3}$, solution. Plotting only the FS results with respect to grid refinement, Fig. 28 shows a convergence of the outflow profile by Mesh C for FS.

The accuracy of FS and FV are compared in Fig. 29, where the outflow solutions from FS and FV are plotted for Meshes C and E. Taking the grid-converged FS Mesh-E solution to be the "truth" solution, it is clear that FS reaches the grid converged solution on a coarser mesh than FV.

Computational efficiencies of the two algorithms are compared in Fig. 30, where the L_2-norm of the residual is plotted versus CPU time for the fine-mesh FS and FV solutions, along with the FS convergence history on Mesh D. The Mesh-E FS solution converges in 760 sec. The corresponding FV solution takes 2.5 times longer than FS, due, in part, to the need to reconstruct gradient information at each node with FV for second-order spatial accuracy. However, considering the solution time to reach a given accuracy, it is more reasonable to compare the FS solution time on Mesh D to the finest-mesh FV solution. The FS Mesh-D solution took only 64 sec, a factor of 29 times less than FV on Mesh E, and still shows better accuracy than the fine-mesh FV solution.

An even greater speedup is seen with FS in conjunction with the van Albada limiter, where now the Mesh-B solution over-plots the curve from the finest grid, shown in Fig. 31. The corresponding FV result using the van Albada limiter on Mesh B is included, and clearly falls short of the FS accuracy. The FV case was repeated with the highly-compressive Superbee limiter with little improvement in accuracy. The solution time for FS on Mesh B is about one second, yielding a speedup factor of 2–3 orders of magnitude over FV.

The final set of results addresses convergence issues while pushing the positivity limits. Figure 32 compares two convergence histories for the second-order FS on Mesh B. The non-converging, though stable, convergence history is the result of using strict positivity arguments to set the timestep (Eqn. 38). The resulting solution is bounded and approximately correct but oscillatory. Limiter "ringing" is considered to be a contributor to this behavior, and the higher-order discretization for the implicit matrix could be reducing the diagonal dominance, and hence stability, of the Gauss-Siedel iteration.

Full convergence is achieved by using first-order positivity coefficients, which are not dependent on the limiters. The resulting local timesteps will not be as large as true second-order positivity would allow, but appear to be more robust.

Summary of Results

Fluctuation splitting and finite volume schemes are compared in detail as applied to scalar advection, diffusion, and advection-diffusion problems. The fluctuation splitting scheme is seen to introduce less artificial dissipation while treating advection terms, allowing for more accurate resolution of weakly dissipative advection-diffusion problems. The ability to resolve solutions to these problems on coarser meshes makes the fluctuation splitting scheme the preferred choice over finite volume.

Linear advection test problems are utilized to investigate the dependence of artificial diffusion production on grid orientation. Both fluctuation splitting and finite volume are shown to exhibit grid dependencies, but with fluctuation splitting producing less artificial dissipation on all grids considered.

A non-linear coalescing shock problem further explores grid dependencies as cases are constructed that result in incorrect shock speeds for finite volume. Fluctuation splitting shows correct shock speeds for all grids and provides tighter shock capturing than finite volume.

An advection-diffusion problem with small physical dissipation (diffusion coefficient of 10^{-3}) is considered where the reduction in artificial dissipation with fluctuation splitting results in a significant accuracy improvement over finite volume. Convergence times are compared, showing a speedup of 2.5 for fluctuation splitting over finite volume on identical grids, using a point Gauss-Seidel relaxation. However, a grid convergence study shows fluctuation splitting has better resolution of the solution on a coarser mesh than finite volume does on finer meshes, resulting is a speedup of 29 for fluctuation splitting over finite volume.

Based upon these significantly reduced solution times for solving model problems, as compared to the current state-of-the-art finite volume method, fluctuation splitting is considered a worthwhile scheme to pursue for modeling fluid dynamic problems.

References

[1]Barth, T. J., "Aspects of Unstructured Grids and Finite-Volume Solvers for the Euler and Navier-Stokes Equations," *Computational Fluid Dynamics*, No. 1994–04 in Lecture Series, von Karman Institute for Fluid Dynamics, 1994.

[2]Mesaros, L. M., *Multi-Dimensional Fluctuation Splitting Schemes for the Euler Equations on Unstructured Grids*, Ph.D. thesis, University of Michigan, USA, 1995.

[3]Sidilkover, D. and Roe, P. L., "Unification of Some Advection Schemes in Two Dimensions," Report 95–10, ICASE, Hampton, Feb. 1995.

[4]Tomaich, G. T., *A Genuinely Multi-Dimensional Upwinding Algorithm for the Navier-Stokes Equations on Unstructured Grids Using a Compact, Highly-Parallelizable Spatial Discretization*, Ph.D. thesis, University of Michigan, USA, 1995.

[5]Carette, J.-C. and Deconinck, H., "Adaptive Hybrid Remeshing and SUPG/MultiD-Upwind Solver for Compressible High Reynolds Number Flows," AIAA Paper 97–1857, May 1997.

[6]Efraimsson, G., "A 2D Analysis of the Influence of Artificial Viscosity Terms on Solutions of the Euler Equations," *Journal of Computational Physics*, Vol. 138, No. 1, Nov. 1997, pp. 103.

[7]Wood, W. A. and Kleb, W. L., "Diffusion Characteristics of Upwind Schemes on Unstructured Triangulations," AIAA Paper 98–2443, Jun. 1998.

[8]Bathe, K.-J., *Finite Element Procedures in Engineering Analysis*, Prentice-Hall, Inc., Englewood Cliffs, USA, 1982.

[9]Roe, P. L., "Approximate Riemann Solvers, Parameter Vectors, and Difference Schemes," *Journal of Computational Physics*, Vol. 43, October 1981, pp. 357–372.

[10]Anderson, W. K. and Bonhaus, D. L., "An Implicit Upwind Algorithm for Computing Turbulent Flows on Unstructured Grids," *Computers and Fluids*, Vol. 23, No. 1, Jan. 1994, pp. 1–21.

[11]Deconinck, H., Roe, P. L., and Struijs, R., "A Mu'tidimensional Generalization of Roe's Flux Difference Splitter for the Euler Equations," *Computers and Fluids*, Vol. 22, No. 2/3, 1993, pp. 215–222.

[12]Sidilkover, D., "A Genuinely Multidimensional Upwind Scheme and Efficient Multigrid Solver for the Compressible Euler Equations," Report 94–84, ICASE, USA, Nov. 1994.

[13]Chakravarthy, S. R. and Osher, S., "High Resolution Applications of the Osher Upwind Scheme for the Euler Equations," AIAA Paper 83–1943, Jun. 1983.

[14]Bruner, C. W. S. and Walters, R. W., "Parallelization of the Euler Equations on Unstructured Grids," AIAA Paper 97–1894, Jun. 1997.

[15]van Albada, G. D., van Leer, B., and Roberts W. W., "A Comparative Study of Computational Methods in Cosmic Gas Dynamics," Report 81–24, ICASE, Hampton, Aug. 1981.

[16]Hirsch, C., *Numerical Computation of Internal and External Flows—Volume 2: Computational Methods for Inviscid and Viscous Flows*, John Wiley & Sons Ltd., 1990.

[17]Spekreijse, S., "Multigrid Solution of Monotone Second-Order Discretization of Hyperbolic Conservation Laws," *Mathematics of Computation*, Vol. 49, 1987, pp. 135–155.

[18]Pirzadeh, S., "Three-Dimensional Unstructured Viscous Grids by the Advancing-Layers Method," *AIAA Journal*, Vol. 34, No. 1, Jan. 1996, pp. 43–49.

[19]Pirzadeh, S., "Progress Toward a User-Oriented Unstructured Viscous Grid Generator," AIAA Paper 96–0031, Jan. 1996.

[20]Smith, R. M. and Hutton, A. G., "The Numerical Treatment of Advection: A Performance Comparison of Current Methods," *Numerical Heat Transfer*, Vol. 5, 1982.

Table 1 Grids and solution times for advection-diffusion problem.

		CPU seconds	
Mesh	Nodes	FS	FV
A	134	< 1	< 1
B	495	1	1
C	1,928	5	8
D	7,529	64	145
E	28,915	760	1880

Table 2 L_2**-norms** $(\times 10^5)$ **of artificial and physical viscosities for advection-diffusion problem.**

FS			FV	
$\|\|\bar{\phi}\|\|_2$ (art.)	$\|\|\phi_v\|\|_2$ (phys.)	Mesh	$\|\|\Phi\|\|_2$ (art.)	$\|\|\phi_v\|\|_2$ (phys.)
1274	215	A	1918	190
597	265	B	640	176
192	161	C	144	119
54	76	D	46	66
13	36	E	18	36

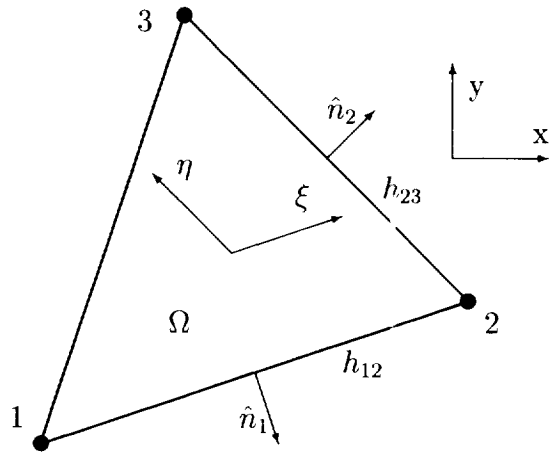

Figure 1 Fluctuation splitting element nomenclature.

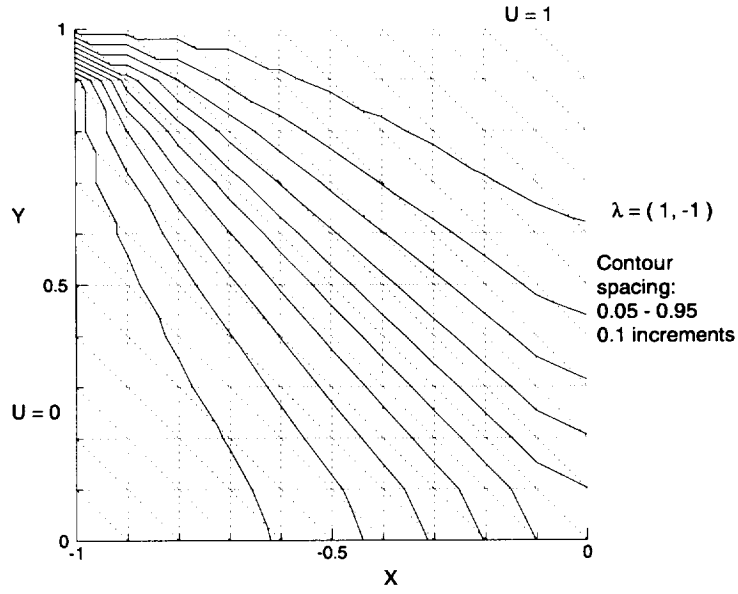

Figure 2 First-order fluctuation splitting, uniform advection.

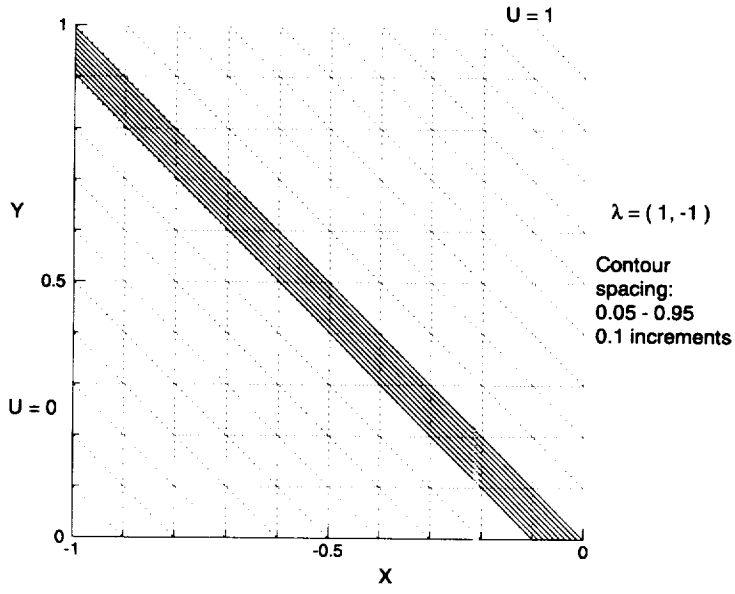

Figure 3 Second-order fluctuation splitting, uniform advection.

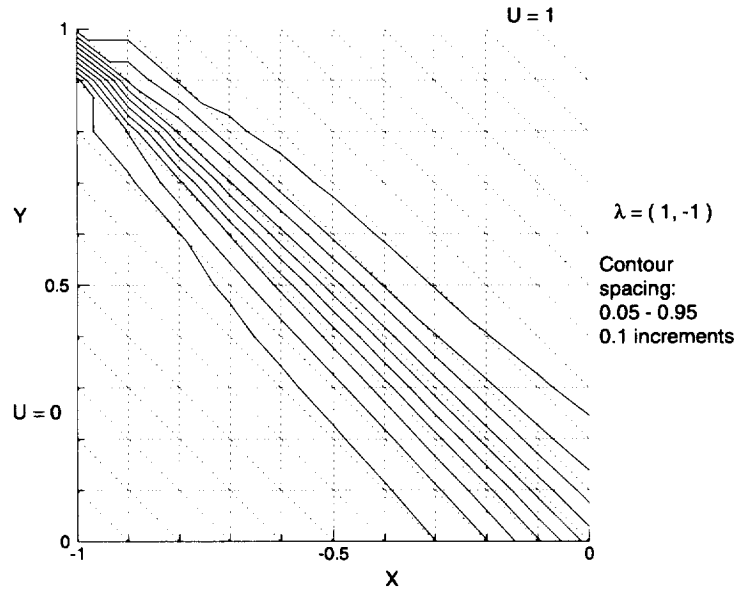

Figure 4 Second-order finite volume, uniform advection.

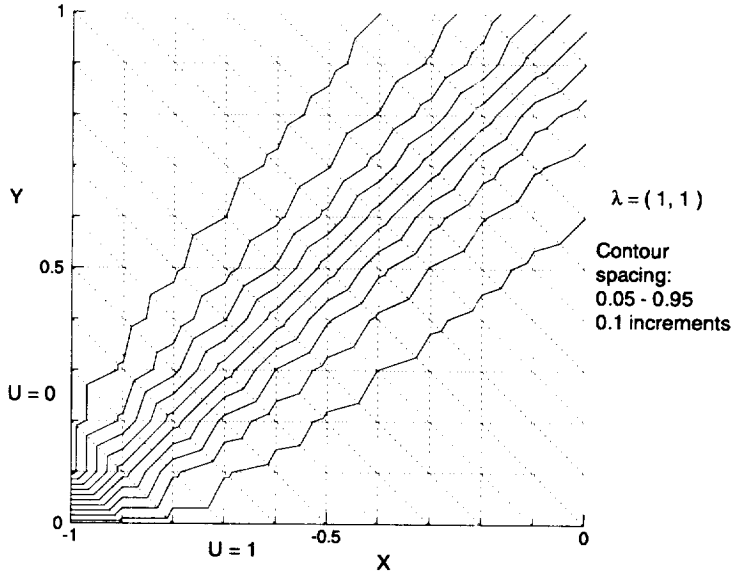

Figure 5 Second-order fluctuation splitting, uniform advection.

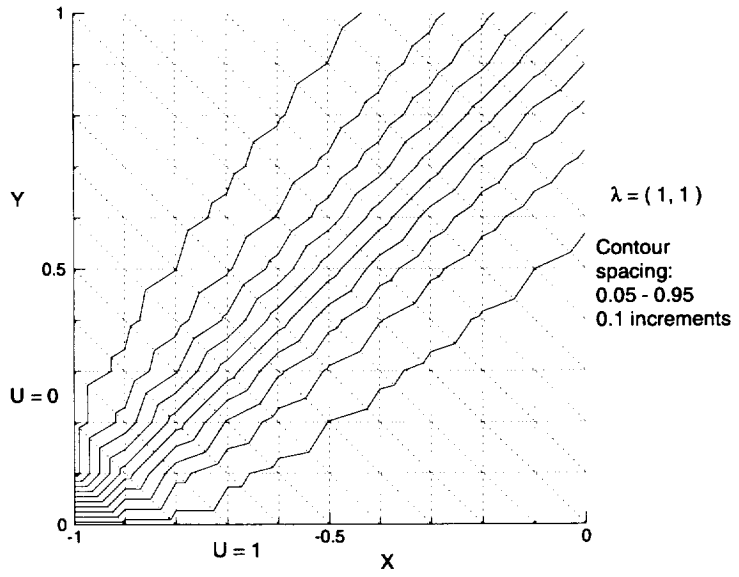

Figure 6 Second-order finite volume, uniform advection.

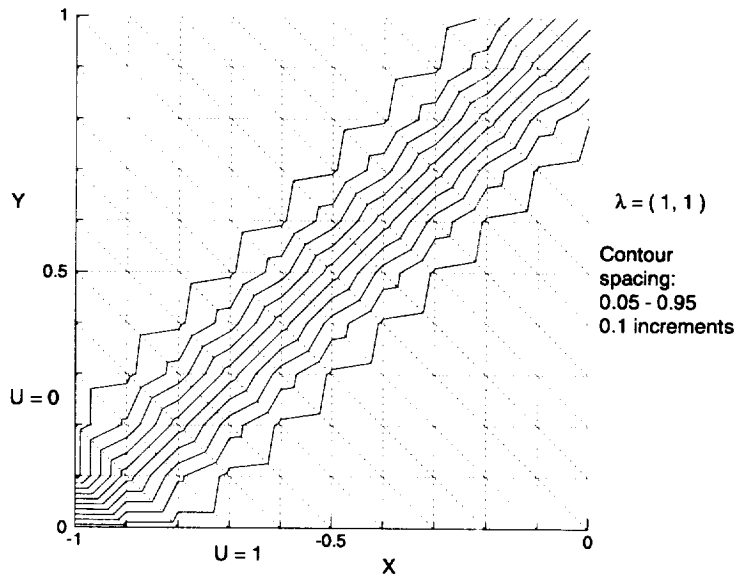

Figure 7 Second-order fluctuation splitting with compressive limiter.

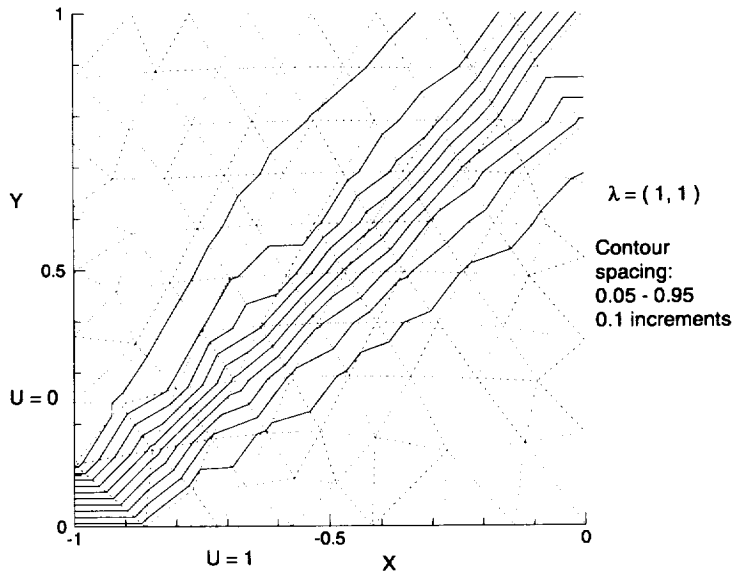

Figure 8 Fluctuation splitting on unstructured mesh.

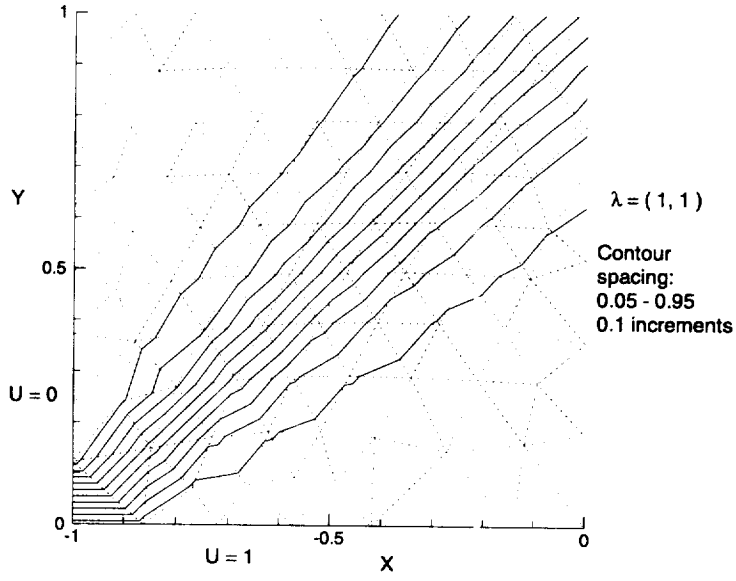

Figure 9 Finite volume on unstructured mesh.

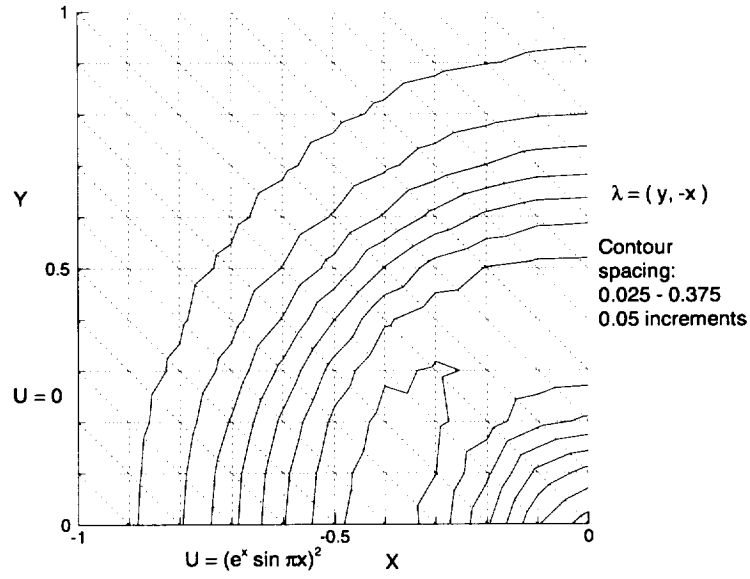

Figure 10 Fluctuation splitting, circular advection.

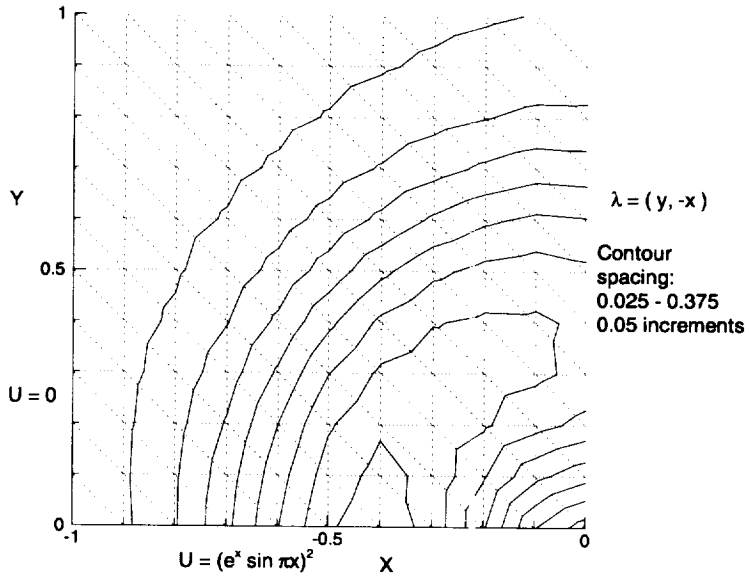

Figure 11 Finite volume, circular advection.

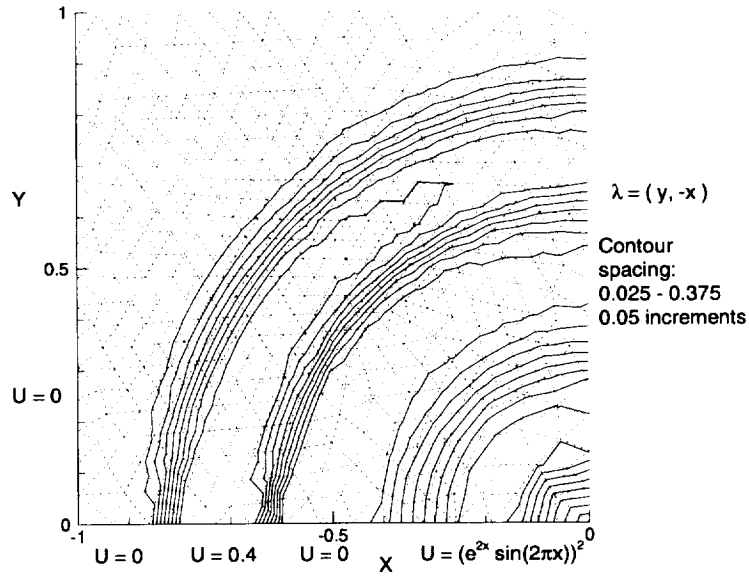

Figure 12 Fluctuation splitting on unstructured mesh, circular advection.

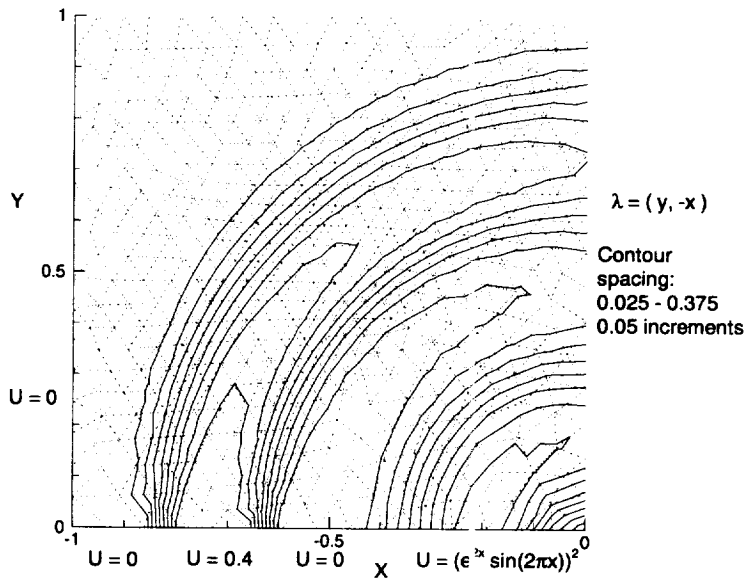

Figure 13 Finite volume on unstructured mesh, circular advection.

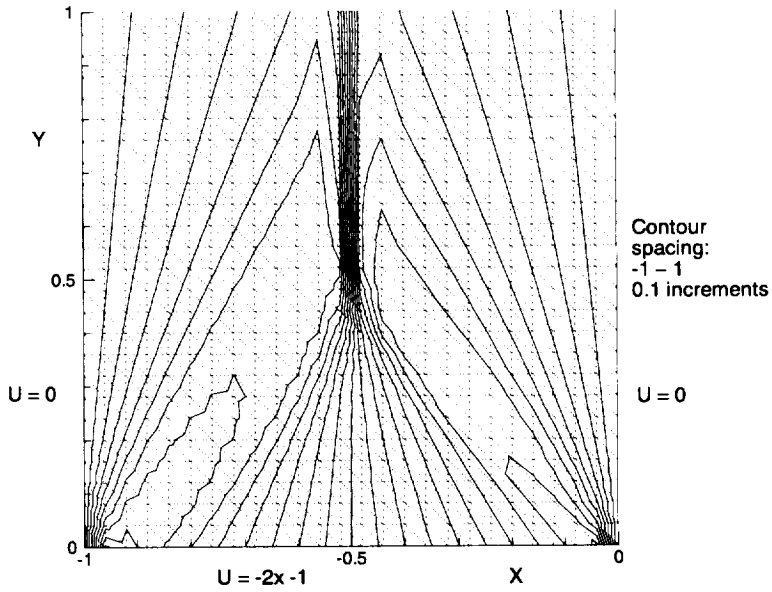

Figure 14 Fluctuation splitting, Burgers equation.

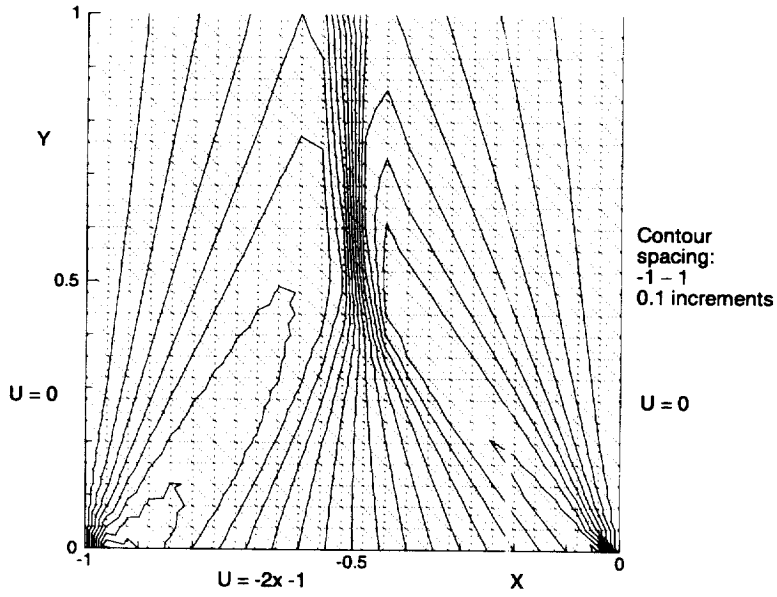

Figure 15 Finite volume, Burgers equation.

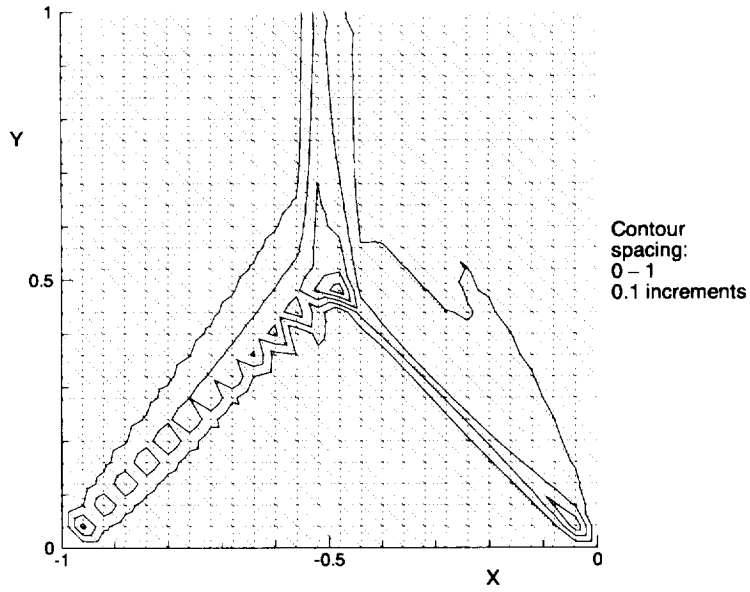

Figure 16 Fluctuation splitting, Burgers equation, absolute error.

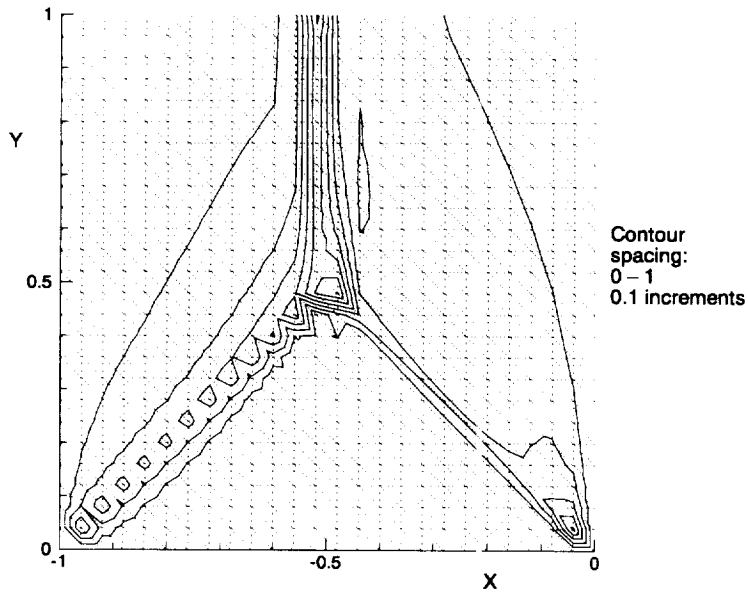

Figure 17 Finite volume, Burgers equation, absolute error.

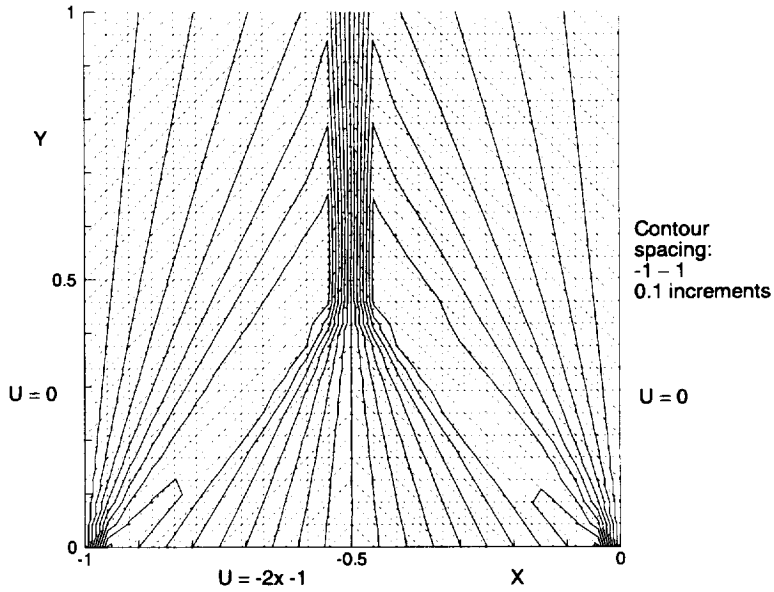

Figure 18 Fluctuation splitting, Burgers equation, symmetric mesh.

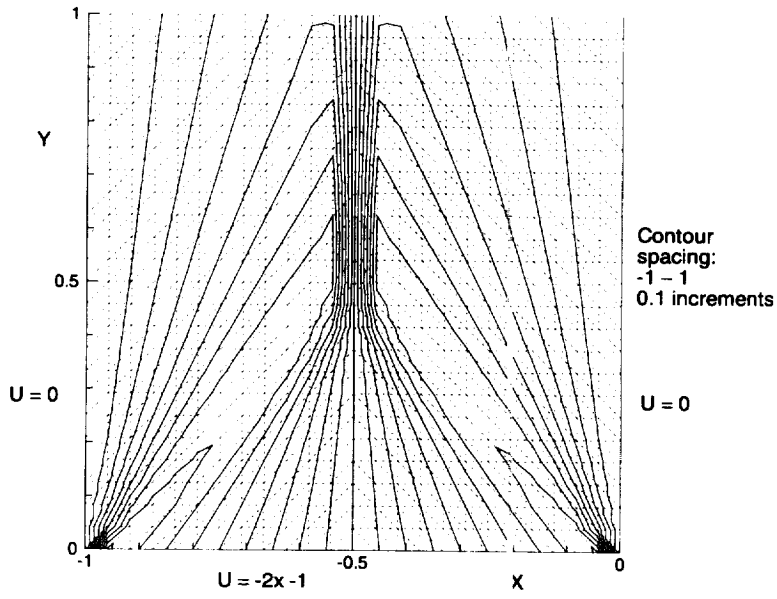

Figure 19 Finite volume, Burgers equation, symmetric mesh.

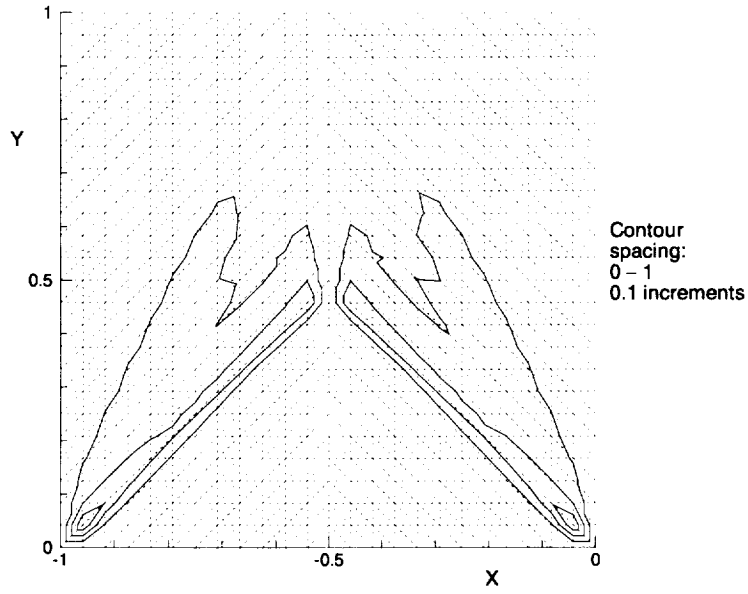

Figure 20 Fluctuation splitting, Burgers equation, absolute error.

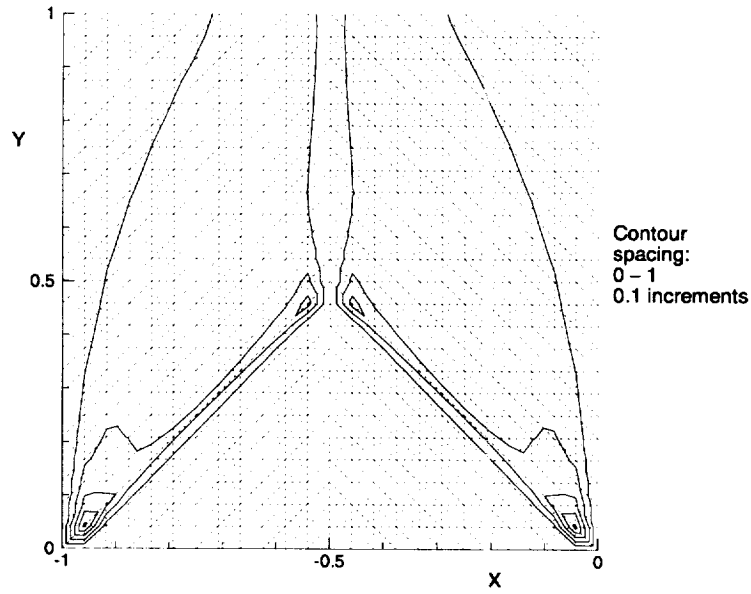

Figure 21 Finite volume, Burgers equation, absolute error.

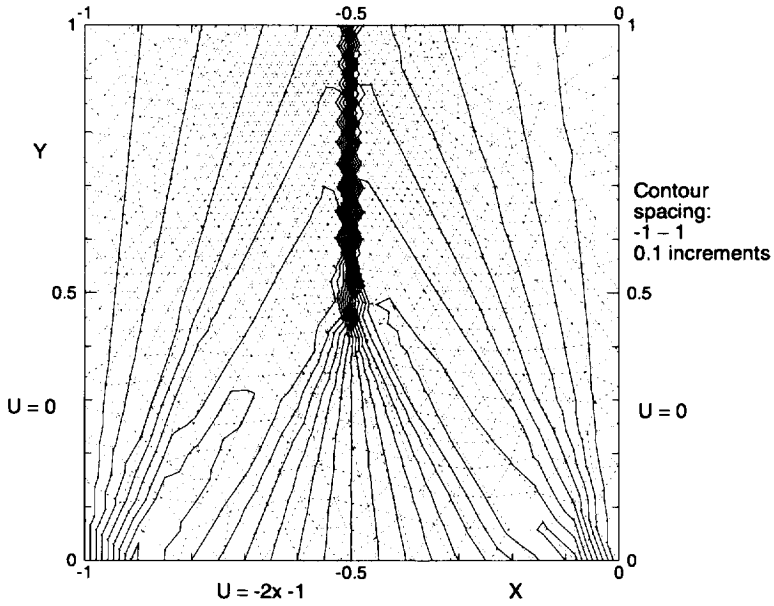

Figure 22 Fluctuation splitting, Burgers equation, unstructured mesh.

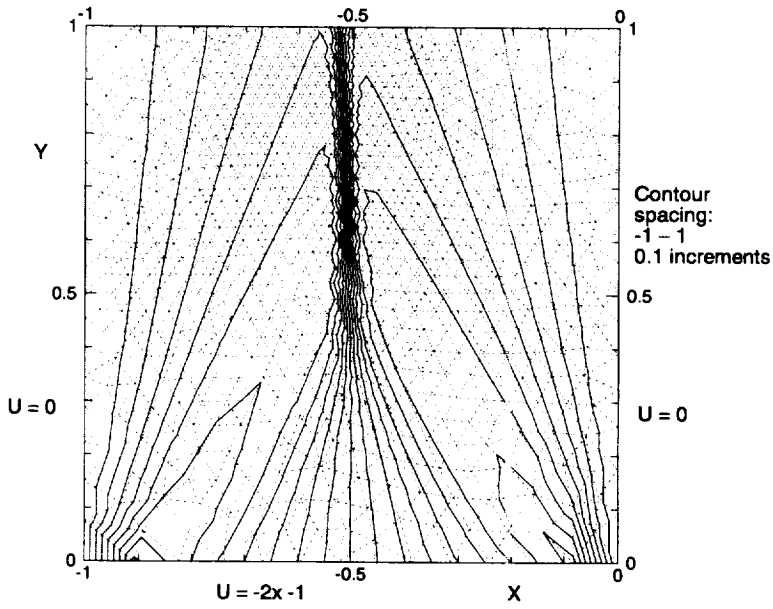

Figure 23 Finite volume, Burgers equation, unstructured mesh.

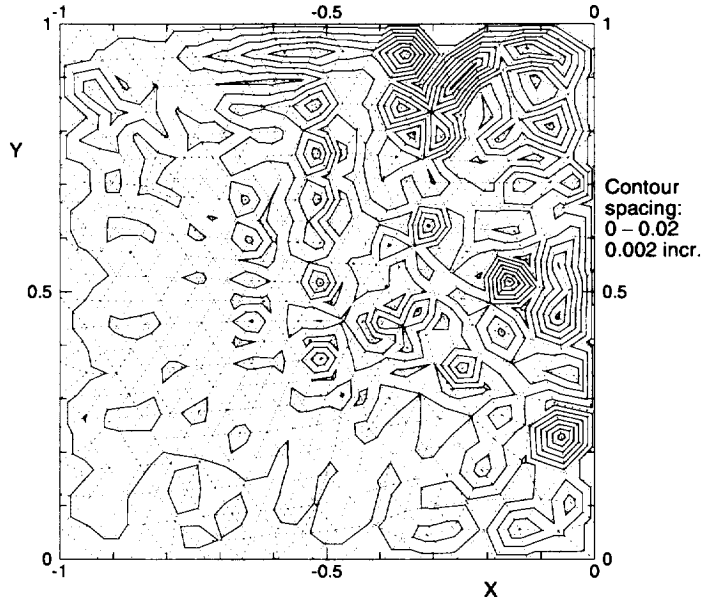

Figure 24 Pure-diffusion problem error, diffusion terms from Eqn. 10.

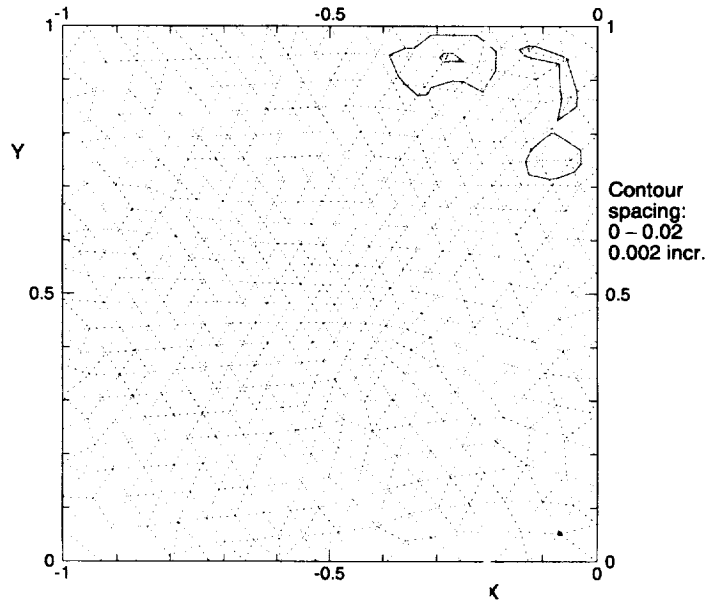

Figure 25 Pure-diffusion problem error, diffusion terms from Eqn. 29.

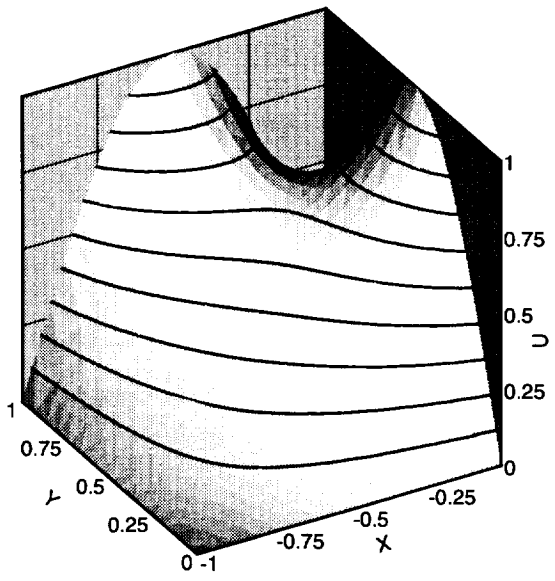

Figure 26 Heat equation solution using finite element formulation. Contour increment is 0.1.

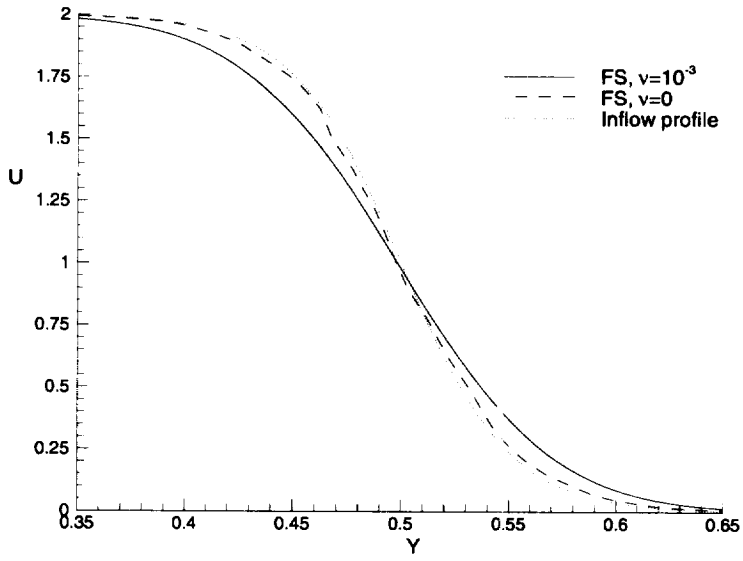

Figure 27 Fluctuation splitting profiles on finest mesh, advection-diffusion problem.

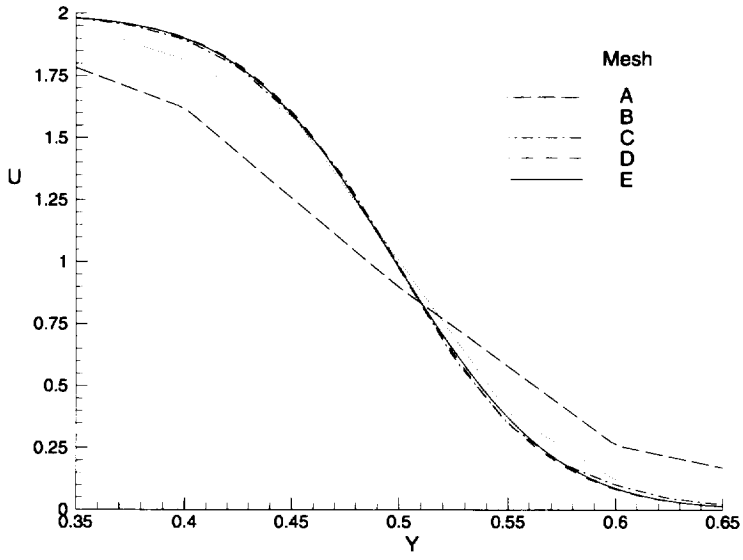

Figure 28 Fluctuation splitting grid convergence, advection-diffusion problem.

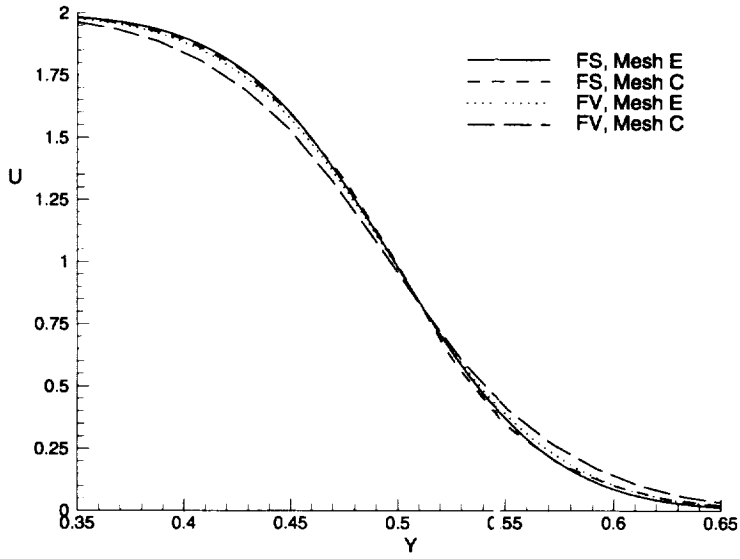

Figure 29 Fluctuation splitting and finite volume for advection-diffusion problem.

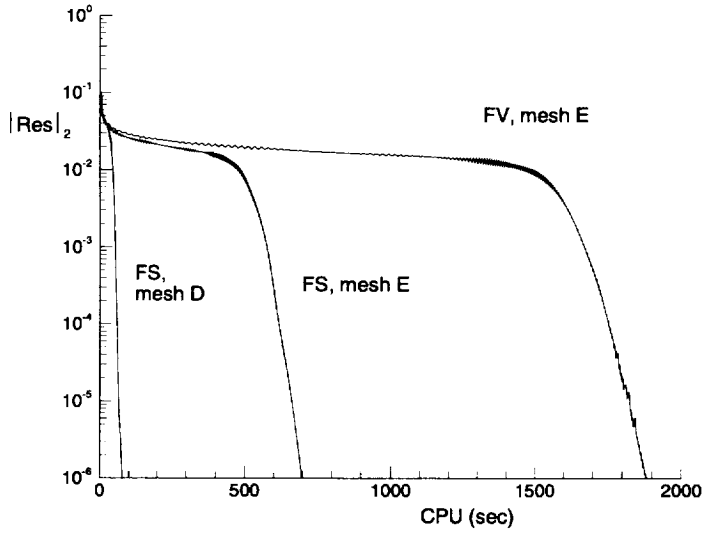

Figure 30 Convergence histories for advection-diffusion problem.

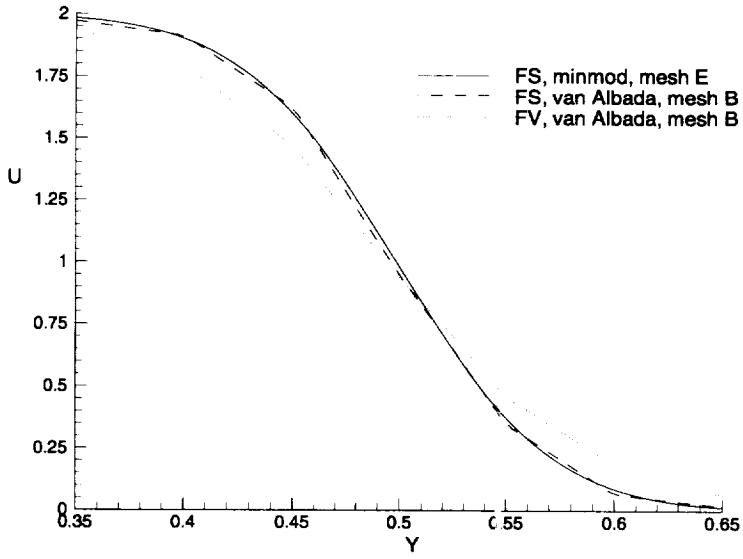

Figure 31 Advection-diffusion results using van Albada limiter.

REPORT DOCUMENTATION PAGE

Form Approved
OMB No. 0704–0188

1. AGENCY USE ONLY *(Leave blank)*	2. REPORT DATE	3. REPORT TYPE AND DATES COVERED
	October 1998	Technical Memorandum

4. TITLE AND SUBTITLE
Comments on the Diffusive Behavior of Two Upwind Schemes

5. FUNDING NUMBERS
WU 242-80-01-01

6. AUTHOR(S)
William A. Wood and William L. Kleb

7. PERFORMING ORGANIZATION NAME(S) AND ADDRESS(ES)
NASA Langley Research Center
Hampton, VA 23681–2199

8. PERFORMING ORGANIZATION REPORT NUMBER
L–17777

9. SPONSORING/MONITORING AGENCY NAME(S) AND ADDRESS(ES)
National Aeronautics and Space Administration
Washington, DC 20546–0001

10. SPONSORING/MONITORING AGENCY REPORT NUMBER
NASA/TM–1998–208738

11. SUPPLEMENTARY NOTES

12a. DISTRIBUTION/AVAILABILITY STATEMENT
Unclassified-Unlimited
Subject Category 64 Distribution: Standard
Availability: NASA CASI (301) 621–0390

12b. DISTRIBUTION CODE

13. ABSTRACT ***(Maximum 200 words)***
The diffusive characteristics of two upwind schemes, multi-dimensional fluctuation splitting and locally one-dimensional finite volume, are compared for scalar advection-diffusion problems. Algorithms for the two schemes are developed for node-based data representation on median-dual meshes associated with unstructured triangulations in two spatial dimensions. Four model equations are considered: linear advection, non-linear advection, diffusion, and advection-diffusion. Modular coding is employed to isolate the effects of the two approaches for upwind flux evaluation, allowing for head-to-head accuracy and efficiency comparisons. Both the stability of compressive limiters and the amount of artificial diffusion generated by the schemes is found to be grid-orientation dependent, with the fluctuation splitting scheme producing less artificial diffusion than the finite volume scheme. Convergence rates are compared for the combined advection-diffusion problem, with a speedup of 2.5 seen for fluctuation splitting versus finite volume when solved on the same mesh. However, accurate solutions to problems with small diffusion coefficients can be achieved on coarser meshes using fluctuation splitting rather than finite volume, so that when comparing convergence rates to reach a given accuracy, fluctuation splitting shows a speedup of 29 over finite volume.

14. SUBJECT TERMS
CFD, Fluctuation Splitting

15. NUMBER OF PAGES
54

16. PRICE CODE
A04

17. SECURITY CLASSIFICATION OF REPORT	18. SECURITY CLASSIFICATION OF THIS PAGE	19. SECURITY CLASSIFICATION OF ABSTRACT	20. LIMITATION OF ABSTRACT
Unclassified	Unclassified	Unclassified	

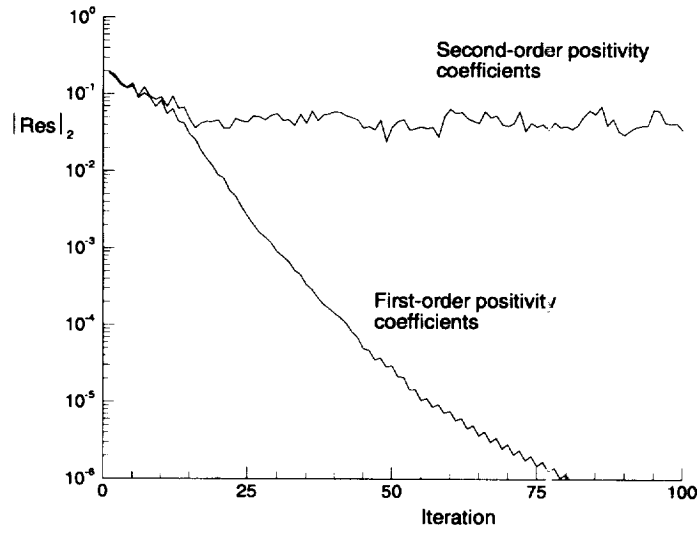

Figure 32 Convergence rates using first- and second-order positivity coefficients.